The Demonstration and Science Experiments Mission: Modeling of Wave Propagation and Triggered Emissions

Michael J Starks[1], Jay M Albert[1], and Dave S Lauben[2]

[1]Air Force Research Laboratory
[2]Department of Electrical Engineering, Stanford University

November 24, 2022

Abstract

The Demonstration and Science Experiments (DSX) mission operated in medium Earth orbit from 25 June 2019 until 31 May 2021. During this time it conducted experiments that actively injected very low frequency waves into the inner magnetosphere to study wave generation, wave propagation, and wave-particle interactions. Experiment planning used cold plasma ray tracing to predict conjunctions for space-to-space transmissions, and the same technique supports post-mission analysis of both monostatic and bistatic signal receptions. Modifications for warm plasma may also be required for extremely oblique waves. In addition, evaluations of amplitude thresholds for triggered emissions provide bounds on DSX signal amplitudes useful for constraining the antenna performance. This report describes both of these analytical tools in the context of mission planning and data analysis. Ongoing analysis using these techniques will be reported in future publications.

The Demonstration and Science Experiments Mission: Modeling of Wave Propagation and Triggered Emissions

M. J. Starks[1], J. M. Albert[1], D. S. Lauben[2]

[1]Air Force Research Laboratory, Kirtland Air Force Base, NM, USA.
[2]Department of Electrical Engineering, Stanford University, Palo Alto, CA, USA.

Key Points:

- Wave transmission by the Demonstration and Science Experiments satellite yielded a wide variety of behaviors
- Whistler mode "boomerangs" were both predicted and observed, and modeled with ray tracing
- Evaluation of a theoretical criterion for nonlinear behavior has implications for any observed triggered emissions

Corresponding author: Michael J. Starks, `michael.starks@spaceforce.mil`

Abstract

The Demonstration and Science Experiments (DSX) mission operated in medium Earth orbit from 25 June 2019 until 31 May 2021. During this time it conducted experiments that actively injected very low frequency waves into the inner magnetosphere to study wave generation, wave propagation, and wave-particle interactions. Experiment planning used cold plasma ray tracing to predict conjunctions for space-to-space transmissions, and the same technique supports post-mission analysis of both monostatic and bistatic signal receptions. Modifications for warm plasma may also be required for extremely oblique waves. In addition, evaluations of amplitude thresholds for triggered emissions provide bounds on DSX signal amplitudes useful for constraining the antenna performance. This report describes both of these analytical tools in the context of mission planning and data analysis. Ongoing analysis using these techniques will be reported in future publications.

1 Introduction

The Air Force Research Laboratory's (AFRL) Demonstration and Science Experiments (DSX) spacecraft (Scherbarth et al., 2009) was launched into a 6000 x 12000 km, 42° inclination orbit on 25 June 2019 and operated until 31 May 2021. The primary DSX mission was to develop technologies for remediating the trapped radiation environment produced by a high-altitude nuclear explosion by exploiting resonant interactions between VLF waves and MeV electrons.

To support these goals, DSX hosted a high-voltage very low frequency (VLF) transmitter (Reinisch et al., 2022) and a sensitive VLF receiver (Linscott et al., 2022) connected to two semi-rigid orthogonal booms with tip-to-tip lengths of 81.6m and 16.3m. The payload also included a three-axis magnetic search coil. During the mission, DSX completed 3,210 orbits and conducted 1,338 active VLF experiments amounting to 28,769 minutes of transmission time and over 10 million individual pulses.

Although VLF transmissions from terrestrial sources have been studied in the Earth's inner magnetosphere for decades (R. A. Helliwell & Katsufrakis, 1979; Inan et al., 1984), DSX represents a rare instance of an active space experiment in which VLF waves are injected *in situ* without intermediating ionospheric plasma. One notable example is the NASA IMAGE mission (Reinisch et al., 2000) which carried a low-power transmitter for magnetospheric sounding that operated down to 3 kHz.

The DSX transmitter was designed to tolerate much higher voltages and was optimized for operations at VLF. To characterize the performance of the transmitter and antenna system, the mission included transmissions to other spacecraft carrying VLF receivers. Ray tracing was utilized during experiment planning to maximize the likelihood of signal reception. In addition to observing natural (such as lightning) and anthropogenic (such as terrestrial transmitter) VLF emissions, DSX captured instances in which its own transmissions reflected back to the spacecraft and these have been successfully explained using ray tracing. Finally, DSX may also have produced unexpected triggered emissions through resonant interactions with trapped electrons. Threshold requirements on wave amplitudes for the triggering process therefore provide insight into the radiation efficiency of the DSX transmitter.

In Section 2 we briefly review ray tracing in cold and warm plasmas using general and quasi-longitudinal treatments. In Section 3 we discuss the use of cold plasma ray tracing to plan DSX conjunctions with terrestrial transmitters and other spacecraft. We also detail its use to predict and explain self-reception of waves transmitted from DSX. Finally, Section 4 analytically examines the conditions needed for DSX to produce secondary, triggered emissions through interactions with energetic electrons along these ray paths. Together these modeling approaches support both mission planning and data analysis.

2 Ray Tracing in Cold and Warm Plasmas

2.1 General Ray Tracing Approach

Since the early days of geophysical studies exploiting VLF waves, ray tracing has been a mainstay for explaining a surprisingly varied repertoire of observations (e.g. Storey (1953)). Ray tracing is an application of geometric optics and a reduction of the Wentzel-Kramers-Brillouin (WKB) approximation to the electromagnetic wave equation solutions via the eikonal approximation (Stix, 1992). This approach effectively treats the wave frequency as infinite and its wavelength as zero. In general that approximation is only valid where the wavelength of the waves being simulated is much smaller than the scale length of variations in the propagation medium, but this applies over a surprisingly large regime in space physics, including that of VLF in the inner magnetosphere.

With these assumptions in place, ray tracing computes the paths of VLF waves using a pair of coupled ordinary differential equations, shown here in the Haselgrove form (Haselgrove, 1963; Budden, 1988):

$$\frac{d\mathbf{r}}{d\tau} = c\frac{\partial G}{\partial \mathbf{n}}, \qquad \frac{d\mathbf{n}}{d\tau} = -c\frac{\partial G}{\partial \mathbf{r}}, \tag{1}$$

where $\mathbf{r}$ represents the ray location in space, $\mathbf{n}$ is the phase index of refraction (which is in the direction of the wave normal), c is the speed of light, and G is the ratio of the magnitude of the state variable $\mathbf{n}$ to the medium's index of refraction at location $\mathbf{r}$ (expected to be equal to 1 at all times). τ is the "ray time", which is not a very useful quantity. In practice the system is typically rewritten in terms of the group time, which describes the propagation of the wave energy.

These equations may be quickly implemented and integrated as an initial value problem using any convenient software package or programming language (e.g. Inan and Bell (1977); Starks (2002)). When combined with plasma density and geomagnetic field models, the solver yields ray positions and wave normals as a function of time.

When tracing whistler mode signals in the magnetosphere it is often found that two key wave normal angles feature in the results: the cold plasma resonance cone angle and the Gendrin angle (Gendrin, 1961), both of which can be derived from the full cold plasma refractive index $n = kc/\omega$, considered as a function of $(\omega_{pe}, \Omega_e, \omega, \theta)$ (the plasma frequency, electron gyrofrequency, wave frequency, and wave normal angle, respectively), e.g., as given by Stix (1992). In the form used by Albert (2005),

$$\frac{1}{n^2} = \frac{(RL - PS)\sin^2\theta + 2PS + \sigma\sqrt{(RL-PS)^2\sin^4\theta + 4P^2D^2\cos^2\theta}}{2PRL} \tag{2}$$

where (R, L, P, S, D) are the standard plasma parameters and σ is defined as the sign of $-PD$, so that $\sigma = +1$ as long as $\omega < \omega_{pe}$ and $\Omega_p < \omega < \Omega_e$. The wave normal angle between the wave vector k and the background magnetic field lies between 0 and 180°, so $k_\perp = k\sin\theta \geq 0$ but $k_\parallel = k\cos\theta$ is signed.

Setting $1/n^2 = 0$ leads to the usual condition $\tan^2\theta_{RC} = -P/S$ for the "resonance cone" angle θ_{RC}, at which the wave index of refraction goes to infinity and beyond which propagation is not permitted.

Propagation is, however, permitted at the Gendrin angle, where the group velocity is initially aligned with the ambient magnetic field (although it need not remain so). The simple relations

$$k_\parallel^2 c^2 = \omega^2 n^2 \cos^2\theta, \quad k_\perp^2 c^2 = \omega^2 n^2 \sin^2\theta, \quad \tan\theta = k_\perp / k_\parallel \tag{3}$$

can be used to express partial derivatives of $k_\perp$ and $k_\parallel$ as derivatives of n^2 with respect to ω and θ. Thus, the expressions for ray propagation can be written as

$$\begin{aligned}
\frac{V_{g\parallel}}{c} &= \frac{1}{c}\Big(\frac{\partial\omega}{\partial k_\parallel}\Big)_{k_\perp} = \Big(n^2\cos\theta + \frac{\partial n^2}{\partial\theta}\frac{\sin\theta}{2}\Big)\frac{1}{\Gamma}, \\
\frac{V_{g\perp}}{c} &= \frac{1}{c}\Big(\frac{\partial\omega}{\partial k_\perp}\Big)_{k_\parallel} = \Big(n^2\sin\theta - \frac{\partial n^2}{\partial\theta}\frac{\cos\theta}{2}\Big)\frac{1}{\Gamma},
\end{aligned} \tag{4}$$

where Γ denotes the combination $n[n^2+(\omega/2)(\partial n^2/\partial\omega)]$ (Albert, 2007, 2008). Setting $V_{g\perp} = 0$ determines the Gendrin angle θ_G and leads to

$$\Big(\frac{RL-PS}{PD}\Big)^2\tan^4\theta_G + 4\tan^2\theta_G + \Big(\frac{RL+P^2}{PS}+2\Big) = 0, \tag{5}$$

which is just a quadratic for $\tan^2\theta_G$. For a whistler mode wave, with $S > 0$ ($\Omega_p < \omega < \omega_{LH}$), $D > 0$ ($\Omega_p < \omega < \Omega_e$), and $P < 0$ ($\omega < \omega_{pe}$), this quadratic has valid solutions unless $L < -P < R$. The condition $L < -P$ is usually satisfied but $-P < R$ is not, and only occurs when, approximately, $\omega > (\Omega_e/2)(1 - \Omega_e^2/2\omega_{pe}^2)$. Thus, the Gendrin angle is not always guaranteed to exist.

2.2 Quasi-Longitudinal Approximation and Parallel Propagation

Simplifying further, the quasi-longitudinal approximation,

$$n^2 = \frac{\omega_{pe}^2}{\omega(\Omega_e|\cos\theta| - \omega)}, \tag{6}$$

can be used for whistler mode waves well above the lower hybrid frequency, giving $\cos\theta_{RC} \approx \omega/\Omega_e$. This yields $\Gamma = (\omega\Omega_e/2\omega_{pe}^2)n^5|\cos\theta|$, as noted by Albert (2017), as well as $\partial n^2/\partial\theta = (\omega\Omega_e/\omega_{pe}^2)n^4\sin\theta$. Combining gives

$$\begin{aligned}
\frac{V_{g\parallel}}{c} &= \frac{1}{n\cos\theta}\Big[1 + |\cos\theta|\Big(|\cos\theta| - \frac{2\omega}{\Omega_e}\Big)\Big] \\
\frac{V_{g\perp}}{c} &= \frac{\sin\theta}{n|\cos\theta|}\Big(|\cos\theta| - \frac{2\omega}{\Omega_e}\Big).
\end{aligned} \tag{7}$$

Note that the parallel components of the wave vector and the group velocity point in the same direction, since $(k\cos\theta)V_{g\parallel} > 0$. Setting the expression for $V_{g\perp}$ to zero gives the standard approximation $\cos\theta_G = 2\omega/\Omega_e$. For $\theta > \theta_G$, n becomes large and $V_{g\parallel}$ becomes small, though it does not go through zero and so does not describe magnetospheric reflection (Kimura, 1966). Indeed, $V_{g\perp} \ll |V_{g\parallel}|$, giving nearly field-aligned propagation. At θ_G this expression for $V_{g\parallel}$ agrees with the estimate of equation 3 of Mourenas et al. (2015), although the latter contains an additional factor of $2(\cos\theta - \omega/\Omega_e)/\cos\theta$, which would imply even smaller values of $V_{g\parallel}$ for $\theta > \theta_G$.

A quasi-longitudinal approach may be taken to simulate propagation in plasmaspheric ducts, which are generally weak (a few percent) field-aligned density enhancements, but may also be depletions (Smith, 1961). Such signals are important because non-ducted waves tend to evolve oblique wave normal angles as they propagate long distances, while those in ducts remain essentially field-aligned. This can be modeled by replacing the Haselgrove equations with a form that ensures the wave refractive index vector (and therefore the wave normal) remains aligned with the ambient geomagnetic field, while enforcing propagation along the field line:

$$\frac{d\mathbf{r}}{dt_g} = \hat{\mathbf{B}}_\mathbf{0} V_g\chi, \qquad \frac{d\mathbf{n}}{dt_g} = \frac{d\mathbf{n}}{d\mathbf{r}}\cdot\frac{d\mathbf{r}}{dt_g} + \frac{d\mathbf{n}}{d\theta}\frac{d\theta}{dt_g}\chi, \tag{8}$$

where $\hat{\mathbf{B}}_\mathbf{0}$ is the direction of the geomagnetic field at location $\mathbf{r}$, t_g is the group time, V_g is the wave group velocity, θ is the wave normal angle, and χ is the sign of $\hat{\mathbf{B}}_\mathbf{0}\cdot\mathbf{n}$. It

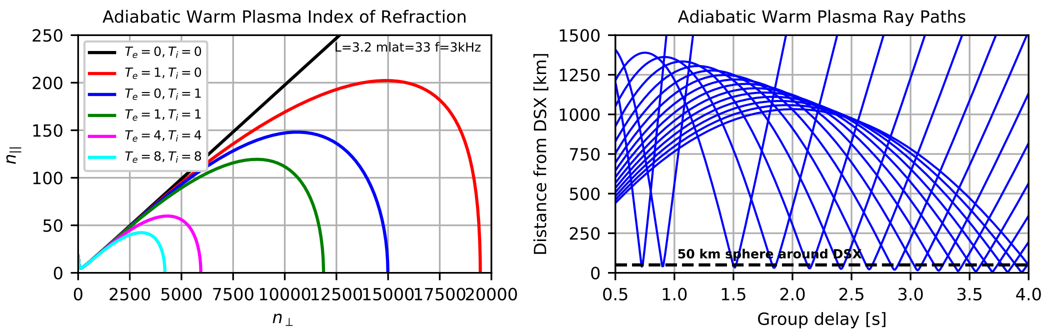

Figure 1. Left: Index of refraction curves for cold and warm plasma. The cold plasma resonance cone is shown in black. Right: Raytracing trajectories in a $T_e = T_i = 1$ eV plasma.

can be shown that $d\theta/dt_g = 0$ because the wave remains field-aligned at all times. In actuality, waves propagate in both ducted and non-ducted modes simultaneously (termed "mixed path" propagation (R. Helliwell, 1965), so both varieties of ray tracing are useful (Starks et al., 2020).

2.3 Warm Plasma Raytracing

It has been suggested that waves emitted from the relatively short DSX antenna may have large indices of refraction, with wave normal angles relatively close to the cold plasma resonance cone. In such circumstances, wave propagation may be better approximated by accounting for warm plasma effects. Aubrey et al. (1970) formulated an adiabatic warm plasma dispersion relation by truncating at the linear term a power series expansion of the moments of the plasma distribution function, noting that this is equivalent to neglecting the divergence of the heat flux. For non-zero ion and/or electron temperatures, this approach eliminates the cold plasma resonance cone and closes the refractive index surface at high values of the index of refraction, as shown in the left panel of Figure 1.

We note that the elimination of the cold plasma resonance cone admits the existence of propagating waves at extreme angles, even in regions forbidden by cold plasma theory. These waves are free to undergo magnetospheric reflection and return to their origins like any other whistler-mode wave.

Maxworth and Gołkowski (2017) conducted ray tracing of oblique waves using the Aubrey formalism to assess the differences in paths, group delays, and damping as compared to cold plasma. In the right panel of Figure 1 we present a group of 3 kHz rays traced in warm plasma from $L = 3.2$ at 33° magnetic latitude. All of these rays are forbidden by cold plasma theory, but in warm plasma they are predicted to return to the transmitter location with a wide range of group delays.

Given the apparent proximity to the cold plasma resonance cone of at least some DSX emitted wave normals, as seen in later in this report, warm plasma ray tracing is likely to play an important role in understanding the performance of the DSX VLF transmitter.

3 Planning Experimental Conjunctions

The DSX mission utilized ray tracing calculations to plan experimental activities, including both VLF transmissions and receptions. The latter category includes VLF en-

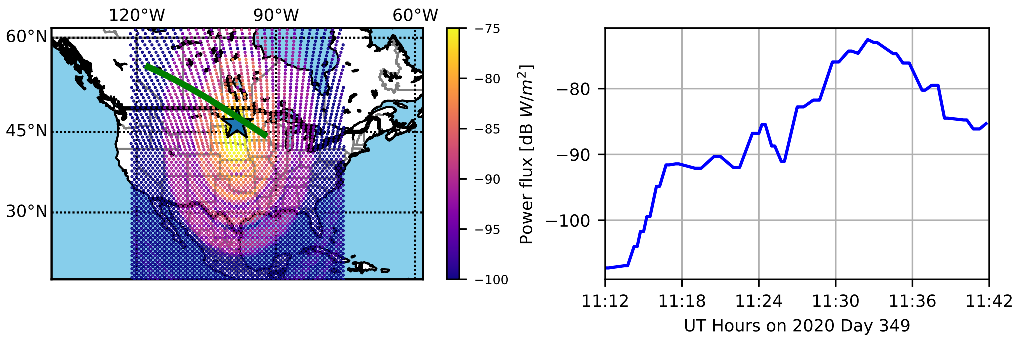

Figure 2. Left: Simulated wave field from 25.2 kHz VLF transmitter at 660 km, with DSX magnetic footprint indicated in green. Right: Predicted power flux at DSX.

ergy produced naturally in the magnetosphere, lightning, and terrestrial transmitters. Plasmaspheric hiss and chorus have known spatial distributions (e.g. W. Li et al. (2015), Aryan et al. (2016), Meredith et al. (2018), Meredith et al. (2020)) that may be compared to the projected DSX ephemeris during experiment planning. Similarly, a lightning VLF climatology is provided by Colman and Starks (2013). Here we consider planning observations of VLF transmissions from ground-based systems and from the DSX spacecraft itself.

3.1 Terrestrial VLF Transmitter Observations

When planning observations of terrestrial VLF transmitters, representations of the transmitter power pattern above the bulk of the ionosphere (such as those found in Cohen et al. (2012)) were ray traced throughout the magnetosphere and virtually "flown through" (Starks et al. (2008)) along the DSX orbital trajectory to identify favorable conjunctions during which to observe the transmitter VLF fields. These power distributions were incorporated into a database built into the DSX planning tools to enable automatic identification of such opportunities. Both ducted and non-ducted ray tracings were included.

The left panel of Figure 2 shows the power flux at 660 km altitude predicted for the 25.2 kHz VLF transmitter in North Dakota, overlaid with the geomagnetic footprint of a portion of a DSX orbit. The right panel indicates the predicted power flux at DSX for non-ducted energy from the transmitter. Actual spacecraft observations will provide information on propagation modes and ionospheric attenuation.

3.2 Space-to-Space Transmissions

The onboard VLF transmitter offers the opportunity to conduct bistatic experiments in which a remote spacecraft listens for DSX signals. The successful reception of DSX transmissions by JAXA's Arase mission (McCollough et al., 2022) demonstrates the utility of ray tracing for space-to-space conjunction planning. Throughout the mission, element sets for DSX and other spacecraft carrying VLF receivers were screened for field-line and line-of-sight conjunctions. When promising opportunities were identified, ray tracing was conducted for times before, during and after the point of closest approach to predict the likely quality of a point-to-point measurement and the best transmit frequency to use.

Figure 3 shows the results of such an analysis during a conjunction in which Arase detected DSX transmissions. The left panel represents a moment when Arase was just 112 km distant from the DSX geomagnetic field line, while the right panel captures the

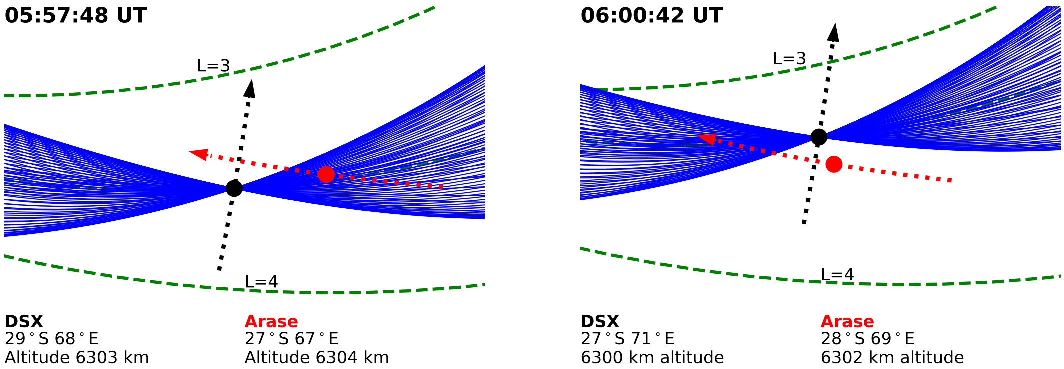

Figure 3. Ray tracing during a DSX conjunction with the Arase spacecraft on 4 Sep 2019.

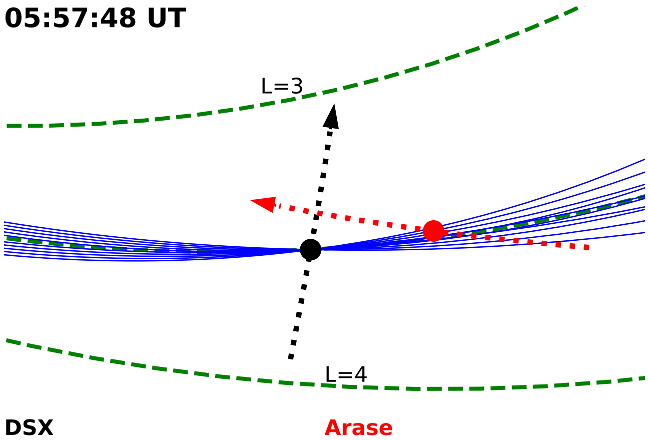

Figure 4. Same as left panel of Figure 3, but restricting the launched wave normal angles.

moment of closest spatial approach between the two vehicles, at 410 km. Ray tracing predicts an Arase reception at the earlier time but not the later one, which agrees with the observations in (McCollough et al., 2022).

Note that these ray tracings propagate all rays with a real index of refraction as determined by the cold plasma dispersion relation. One of the goals of DSX was to investigate the behavior of its 82 m antenna emitting VLF waves in a magnetoplasma and to identify a serviceable model of antenna performance. By considering all admissible rays, observations of when rays are and are not detected by the listening spacecraft and any noted Doppler shifts can help to determine which wave normal angles are actually excited from the DSX antenna.

As an example, Figure 4 reproduces the analysis in the left panel of Figure 3 while restricting the launched wave normal angles to high values at or above the Gendrin angle (79° in this case). We note that the extent of the illuminated region becomes much smaller – an effect that, if present, should be observable in the Arase data.

The matter of emitted wave normals becomes more significant when analyzing conjunctions with spacecraft in low Earth orbit, such as AFRL's VLF Propagation Mapper (VPM) smallsat, which carried a VLF receiver (Marshall et al., 2021). VPM operated in a circular 500 km, 52° inclination orbit and was a target for DSX VLF transmis-

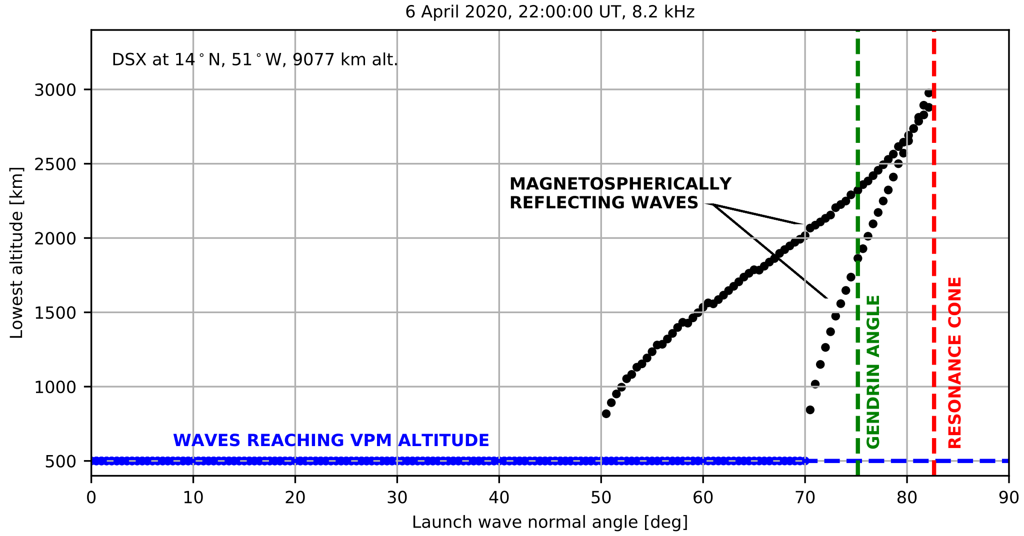

Figure 5. Reflection altitudes for DSX transmissions to VPM.

sions between February and September 2020. Similar to the case with spacecraft at higher orbits, element sets were screened throughout the mission for geomagnetic field line conjunctions. Ray tracing was then performed at a variety of frequencies to identify the transmitter settings most likely to result in a reception. At mid-band frequencies (∼10 kHz) some of the admissible wave normal angles result in rays that are predicted to undergo magnetospheric reflection before reaching VPM altitudes. Reflection may occur when a whistler-mode wave propagates into a region where the wave frequency is below than the local lower hybrid frequency. At this point the cold plasma resonance cone disappears, the refractive index surface closes, and the wave normal may reverse its sense with respect to the geomagnetic field. This is the case for all low-band frequencies (∼3 kHz), but does not occur for high-band (∼20 kHz). Thus, receiving or not receiving DSX transmissions on VPM can in conjunction with ray tracing provide evidence for the presence or absence of ranges of wave normal angles in the emitted radiation (Reid et al., 2022).

Figure 5 depicts the lowest altitudes reached by 8.2 kHz VLF emissions from DSX during a field-line conjunction with the VPM spacecraft, as predicted by ray tracing. It captures the behavior of all admissible rays, and shows that for small wave normal angles, energy is expected to penetrate to the VPM altitude where it might be detected. At larger angles, the waves magnetospherically reflect at higher altitudes. For clarity, there are two traces plotted in black in the figure, corresponding to waves in the meridional plane launched toward and away from the Earth. In reality, waves with other azimuths around the geomagnetic field line smoothly fill the region between the two traces shown. See Reid et al. (2022) for an analysis of all of the DSX-VPM experiments.

3.3 Boomerang Receptions

As described above, whistler mode waves such as those emitted from DSX may under certain circumstances undergo magnetospheric reflection and reverse their path along the geomagnetic field. A subset of those reflected waves may return to DSX and be detected, thereby providing a self-diagnostic capability.

Figure 6 shows an example boomerang experiment, during which DSX was near $L = 2$ and just south of the geomagnetic equator. The top panel will be discussed presently,

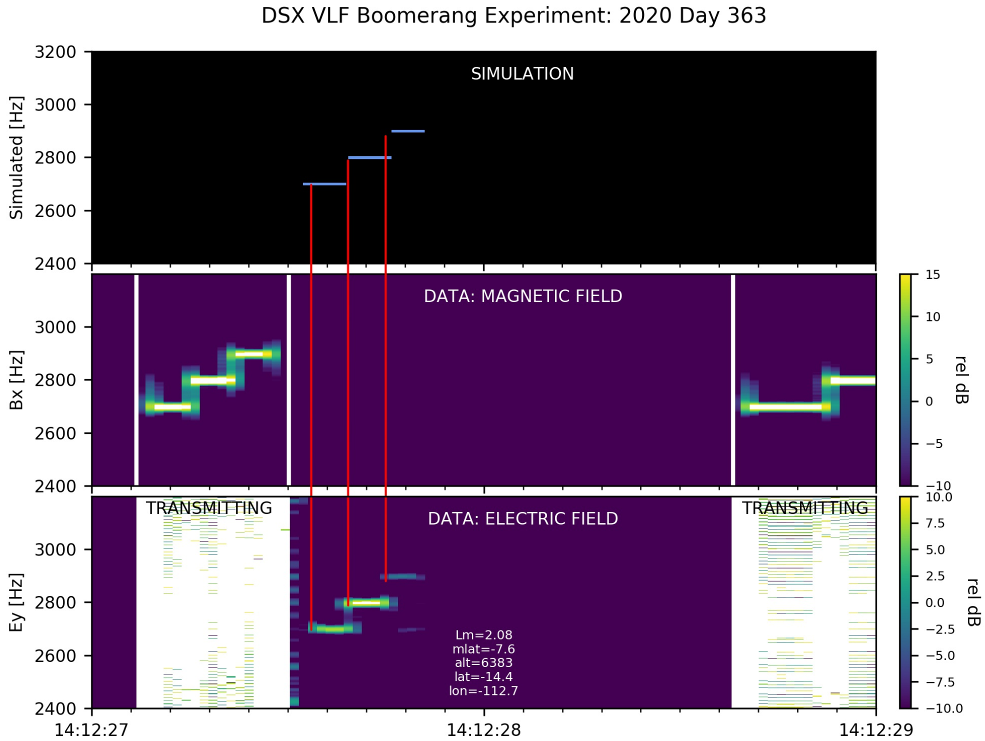

Figure 6. Simulated and observed DSX boomerang spectrograms.

but the lower two panels show data from the BBR, including periods when DSX was transmitting (between the white bars) and listening. At 14:12:27 UT, DSX transmitted three 100 ms pulses at 2700, 2800 and 2900 Hz, which are clearly seen as leakage in the magnetic field channel depicted in the center panel. The electric field channel (bottom panel) is saturated during the transmission. Boomerang echoes are detected in the electric field after a short delay, but are not seen in the magnetic field.

Cold plasma ray tracing may be used to understand these observations and learn something about which waves are emitted by the DSX transmitter. 10,000 rays at 2800 Hz were launched both north- and south-bound from the DSX location with wave normal angles arrayed between field-aligned and nearly 90° to the geomagnetic field (i.e. near the resonance cone) with a maximum index of refraction of 670. This index of refraction corresponds to a wave with a 160 m wavelength, which would be favored by the DSX antenna in the vacuum approximation. A full 360° set of azimuths around the geomagnetic field was included in the simulation. Although waves at a single wave normal angle look the same to the antenna (to first order) and plasma regardless of their azimuth, they incur different Doppler shifts due to the orbital motion of DSX and travel slightly different paths. A fully three-dimensional simulation is therefore required, and this was performed in an eccentric dipole magnetic field based on IGRF coefficients (Alken et al., 2021). The Ozhogin plasmaspheric density model was linearly scaled to match the plasma density observed at the DSX location by analyzing DSX spectrograms using the method described in Reinisch et al. (2022).

Figure 7 captures the results of the ray tracing, where only the rays returning to within 20 km of the DSX location are considered candidates for boomerang reception. The bottom panel plots the index of refraction at launch of all of the returning rays as a function of their initial wave normal angle. Because all of the returning waves have very

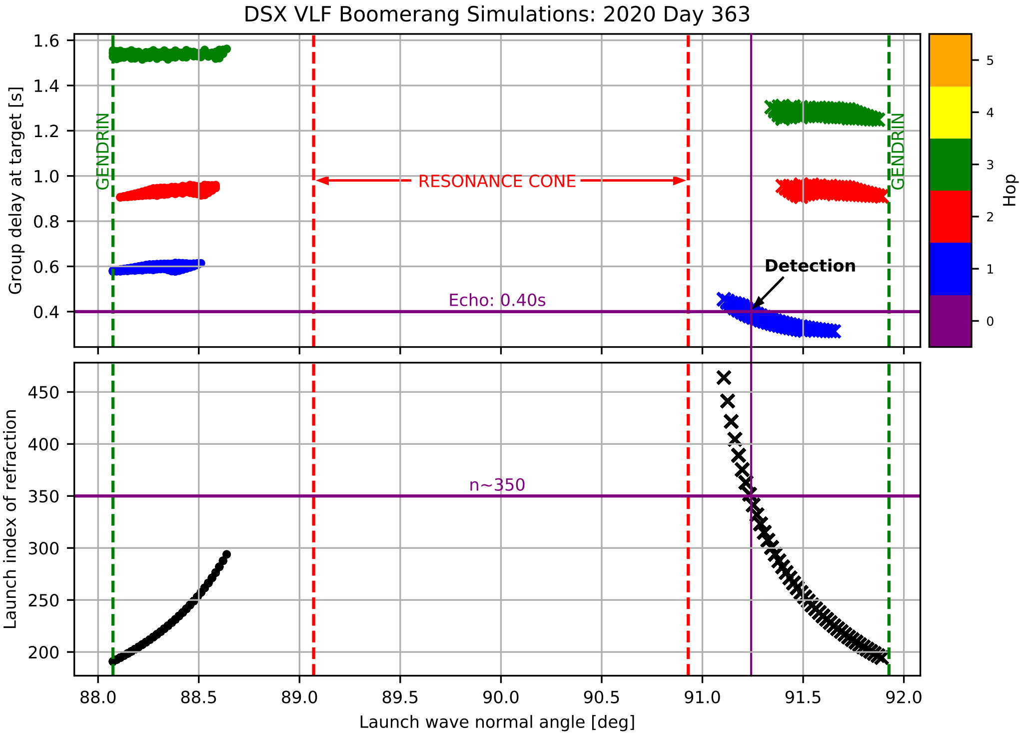

Figure 7. Parameters of predicted 2800 Hz boomerang rays. The middle of the horizontal axis (*i.e.* 90°) is perpendicular to the geomagnetic field. Note the predicted boomerang detection where the purple lines cross.

high initial wave normal angles ($> 88°$) the plot conveniently captures rays initially launched both northward (left half of plot) and southward (right half). For reference, the cold plasma resonance cone angle is depicted by dashed red lines. Propagation is forbidden in the region between them. The Gendrin angle at which rays initially propagate directly along the geomagnetic field line is marked with green dashed lines.

We observe that southbound rays with wave normal angles in a narrow range ($<\sim 1°$) are predicted to return to DSX, with indices of refraction between about 200 and 450. This is the short path to the mirror point, as DSX was at a magnetic latitude of $-7.6°$. The somewhat longer path to the north results in a more limited – but similar – set of predicted boomerang receptions.

The top panel of Figure 7 plots the round-trip transit time to DSX of the predicted boomerang signals, again as a function of launch wave normal angle and color coded by "hop" (one hop corresponds to a trip to the mirror point and back; two hops involve travel onward to the conjugate mirror point and return to DSX; and so on). We note three hops are predicted within the 4 seconds that were simulated, and that the northbound rays with the longer paths have longer delays for odd hops (the red, two-hop times are the same because the path lengths are the same for even hops).

Returning to Figure 6, we observe that the 2800 Hz pulse was seen back at DSX after an 0.4s propagation delay. Adding the purple line at 0.4s to Figure 7, we identify an intersection with only the southbound rays, corresponding most closely to an index of refraction (n) of 350. No corresponding northbound rays with this index of refraction are predicted to return to DSX, and indeed none appear in the data. If such rays were observed, one would expect a distinct echo at 0.6 s (based on the top panel of Figure 7), well-separated from the other return.

As a final step, ray tracing is performed for all three transmitted frequencies using the same approach to select the initial wave normal angle. That is, each pulse is treated as an individual experiment, because the behavior of the DSX antenna in the plasma is not well-understood. The top panel of Figure 6 is a synthetic spectrogram created from the predicted boomerang rays, accounting for transmit and receive Doppler shifts. We note that it reproduces the observations at all three frequencies with about 10% accuracy, which is impressive over path lengths of 10s of Mm.

We make three important observations from these results:

1. The time of arrival of the first southbound hop (blue markers, right side of Figure 7) has a moderate dependence on the launch wave normal angle. If all of the depicted waves were excited by the antenna, about $0.08/0.40 = 20\%$ time dispersion would be expected in the observed boomerang. This amount is resolvable, but is not seen. This constrains the possible wave normal bandwidth of the transmission.

2. At wave normal angles larger than about $91.4°$, the simulation predicts multiple hops returning to DSX. These are not observed. If waves with such wave normals were emitted, it would be surprising not to see those later echoes, given the relatively short path lengths and the strength of the first-hop signal. It would also imply that corresponding northbound waves should be observed, including a one-hop boomerang. These are also not observed. This suggests a quite narrow range of possible wave normal angles emitted by DSX in this case: about $0.5°$ centered near $91.2°$.

3. The magnetic field channel in the center panel of Figure 6 shows no detectable magnetic field signature from the boomerang reception. The quasi-electrostatic nature of the wave so implied strengthens our conclusion that highly-oblique waves near the resonance cone are in fact responsible for the detected signals. However, these waves are still not oblique enough that warm plasma ray tracing (as described in Section 2.3) yields different results from cold plasma, so those results are not shown.

This technique is quite sensitive to wave normal angle because of the steepness of the refractive index surface near the cold plasma resonance cone. Figure 8 plots three rays from Figure 7 with very similar wave normal angles. Each panel shows distance from DSX and magnetic latitude as a function of time. Rays passing within 20 km of DSX are considered candidates for reception (horizontal dotted line). Panel A represents the southbound ray with the matching first-hop transit time, and it can be seen that it exactly matches the observed delay on the first hop (red circle) but does not return within 20 km of DSX on later hops. Panel B depicts a ray with a slightly different wave normal angle, which returns to DSX on the first, second and third hops, but much too quickly as compared to the data. We conclude that the antenna did not excite this wave normal. Panel C shows a ray with wave normal angle to the geomagnetic field almost identical to that in Panel 1, but launched northbound. Note that it never returns to DSX.

A larger study of DSX boomerang receptions conducted in this manner should yield constraints on the nature of the waves emitted during the active experiments, although it only addresses those wave normal angles corresponding to waves that have paths back to DSX.

4 Triggered Emissions: Inhomogeneity Parameter for Oblique Whistler Waves

With a methodology for understanding ray paths and endpoints, we turn now to interesting phenomenology that may transpire along that propagation path, and in par-

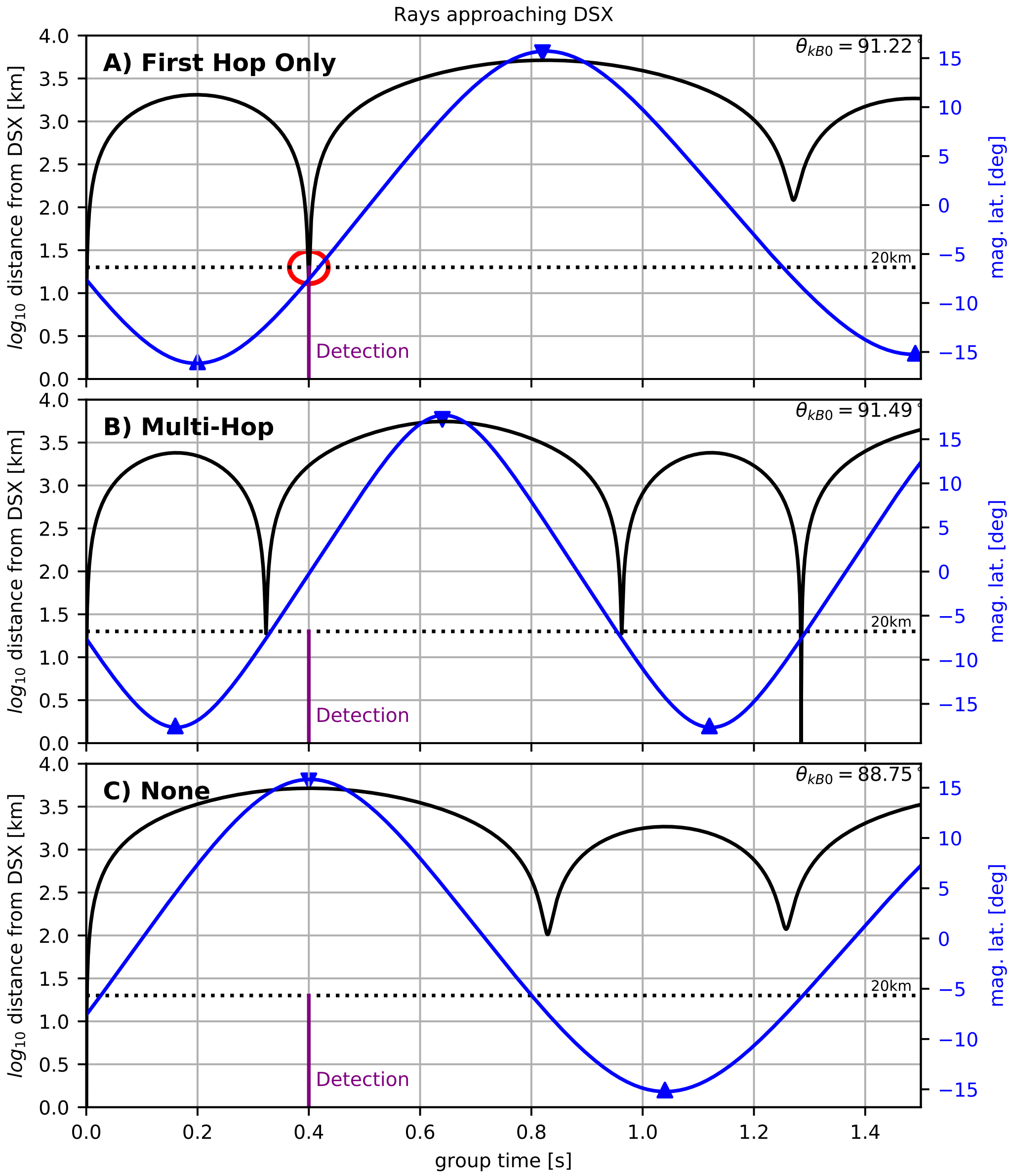

Figure 8. Distance from DSX and magnetic latitude of three 2800 Hz rays. The 20 km detection radius is indicated, as is the time at which the boomerang was detected. Magnetospheric reflections are indicated by the blue triangles. Note potential detection at red circle in Panel A.

ticular triggered emissions. It is well known that the introduction of an appropriate coherent VLF wave into the magnetosphere, under fortuitous conditions, can generate or "trigger" additional wave activity, with differing time-frequency characteristics. The resulting wave amplitude can exceed that of the triggering wave, since the energy is mostly supplied by the underlying plasma. A brief review of triggered emissions generated by the transmitter at Siple Station, Antarctica between 1973 and 1988 is given by (J. D. Li et al., 2015).

The controlled nature of the DSX transmitter offers a unique opportunity to study such processes, which are inherently nonlinear. Though this is still an active and unsettled field of research, virtually all theoretical analysis takes as its point of departure the so-called "inhomogeneity parameter" R (Gołkowski et al., 2019; Tao et al., 2020), which may be interpreted as either the direct ratio of linear to nonlinear terms in a pendulum-like evolution equation or as the ratio of timescales for resulting adiabatic and nonlinear trajectories (Albert, 1993; Tao et al., 2020). A prerequisite for nonlinear behavior, including triggered emissions, is $R < 1$. The amplitude of the triggering wave is a crucial ingredient, though the plasma and resonant particle parameters are also important.

We consider a relativistic particle near resonance with a single whistler-mode wave with arbitrary wave normal angle θ. The phase angle ξ is a combination of the wave and gyro phases, $\xi = \xi_0 + k_\parallel \zeta - \omega t + s\ell\phi$, where ζ is distance along the magnetic field line, s is the sign of the particle charge ($s = -1$ for electrons), and the integer ℓ specifies the resonance. Following the usual treatment (Bell, 1984; Omura et al., 2008; Mourenas et al., 2015), we write the lowest-order equation for $d\xi/dt$ as

$$\frac{d\xi}{dt} = k_\parallel v_\parallel + s\ell \frac{\Omega_e}{\gamma} - \omega, \tag{9}$$

which is zero at resonance, and develop an expression for $d^2\xi/dt^2$. Allowing ω and $k_\parallel$ to depend on t and ζ,

$$\frac{d^2\xi}{dt^2} = k_\parallel \frac{dv_\parallel}{dt} + \frac{dk_\parallel}{dt} v_\parallel + \frac{s\ell}{\gamma}\frac{\partial \Omega_e}{\partial \zeta}\frac{d\zeta}{dt} - \frac{s\ell\Omega_e}{\gamma^2}\frac{d\gamma}{dt} - \frac{d\omega}{dt}. \tag{10}$$

Expressing $dv_\parallel/dt$ in terms of $dp_\parallel/dt$ and $d\gamma/dt$, using $d\zeta/dt = v_\parallel$, and taking the gyro-averaged expressions for $dp_\parallel/dt$ and $d\gamma/dt$ from Albert et al. (2013) gives

$$\begin{aligned} \frac{d^2\xi}{dt^2} &= \Big(\frac{dk_\parallel}{dt} v_\parallel - \frac{d\omega}{dt}\Big) + \Big(s\ell v_\parallel - \frac{k_\parallel v_\perp^2}{2\Omega_e}\Big)\frac{\partial \Omega_e}{\partial \zeta} + \omega_{NL}^2 \cos\xi \\ &\equiv \omega_{NL}^2 \big(R + \cos\xi\big), \end{aligned} \tag{11}$$

where R is the inhomogeneity parameter. The squared nonlinear trapping frequency is

$$\omega_{NL}^2 = \frac{|q|}{mc\omega}\frac{\omega^2}{\gamma}\Big(\frac{k_\parallel^2 c^2}{\omega^2} - 1\Big)\Big\{\frac{v_\perp}{c}\Big[\frac{E_1+E_2}{2}J_{\ell+1} + \frac{E_1-E_2}{2}J_{\ell-1}\Big] - s\frac{v_\parallel}{c}E_3 J_\ell\Big\}, \tag{12}$$

and the Bessel functions J have argument $k_\perp \rho$. The wave electric field components have ratios

$$\frac{E_1}{E_3} = \frac{P - n^2\sin^2\theta}{n^2\cos\theta\sin\theta}, \qquad \frac{E_2}{E_3} = -\frac{D}{S-n^2}\frac{E_1}{E_3}, \tag{13}$$

the squared, time-averaged wave amplitude is $E_w^2 = (E_1^2 + E_2^2 + E_3^2)/2$, and the corresponding wave magnetic field components (in cgs units) are

$$B_1 = nE_2\cos\theta, \quad B_2 = n(E_1\cos\theta + E_3\sin\theta), \quad B_3 = nE_2\sin\theta. \tag{14}$$

The time derivatives are convective derivatives following the particle: $d()/dt = \partial()/\partial t + v_\parallel \partial()/\partial\zeta$. Along a dipole field line, distance ζ and latitude λ are related by $d\zeta/d\lambda = L\cos\lambda\sqrt{1+3\sin^2\lambda}$, which may be integrated to

$$\zeta = \frac{L}{2\sqrt{3}}\Big[\sqrt{3}\sin\lambda\sqrt{1+3\sin^2\lambda} + \log\Big(\sqrt{3}\sin\lambda + \sqrt{1+3\sin^2\lambda}\Big)\Big]. \tag{15}$$

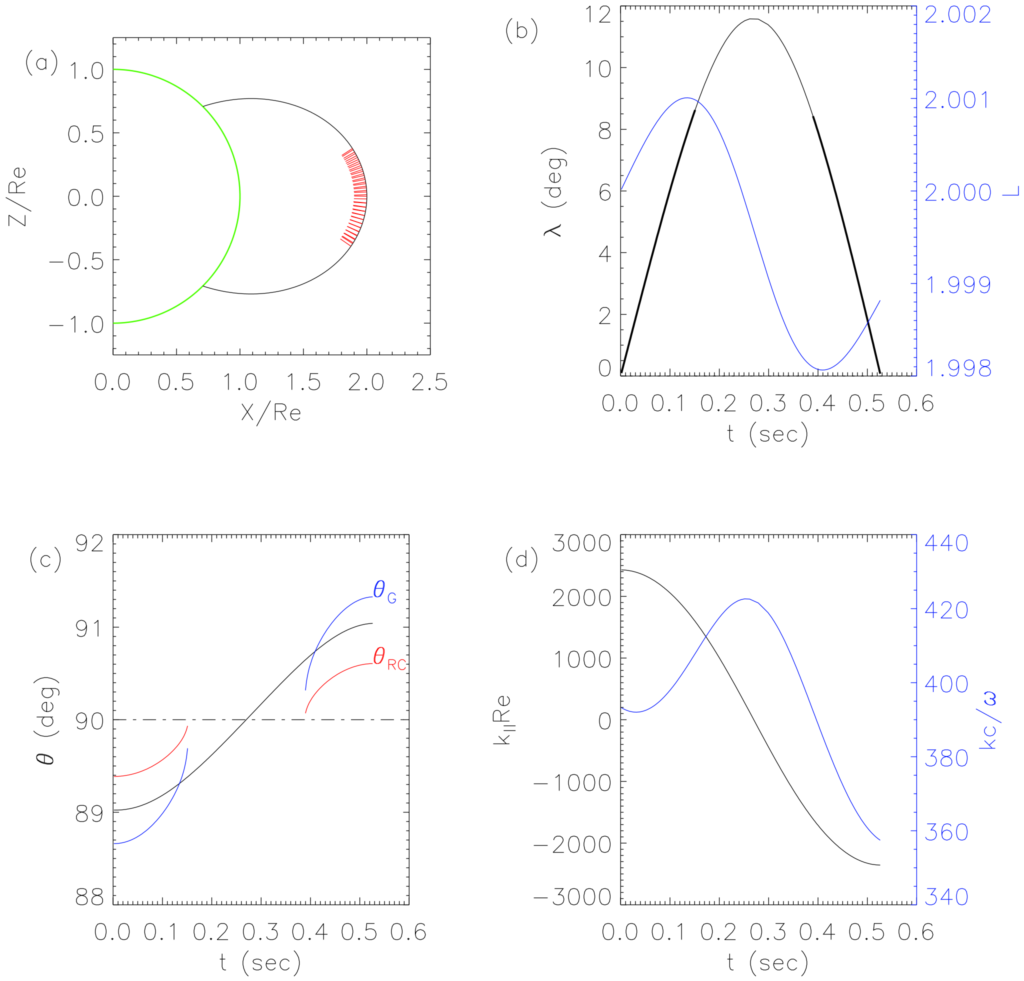

Figure 9. Ray tracing of a single wave in a simple dipole at $L = 2$ with $n_e = 2850$ cm^{-3}, starting at the equator. Initially the wave frequency is slightly above the lower hybrid frequency ($\omega/\omega_{LH} = 1.1$), and the wave normal angle is halfway between the Gendrin and resonance cone values. (a) Trajectory, with red marks indicating the direction of the wave vector. (b) Magnetic latitude and dipole L value vs. time (until recrossing the equator). (c) Wave normal angle θ, local Gendrin angle θ_G, and local resonance cone angle θ_{RC} vs. time. (d) Values of $k_\parallel$ and refractive index vs. time.

4.1 Terms Involving Time Dependence

Allowing ω to depend on t requires several modifications. It is assumed that the frequency variation of the wave originates at its localized source, from which the wave propagates while obeying

$$\frac{\partial \omega}{\partial t} + (V_g \cdot \nabla)\omega = 0. \tag{16}$$

If V_g points mostly in the ζ direction, as it does for both $\theta = 0$ and the Gendrin angle θ_G, then $\partial\omega/\partial\zeta \approx -(\partial\omega/\partial t)/V_{g\|}$ and $d\omega/dt \approx (1 - v_\|/V_{g\|})(\partial\omega/\partial t)$. Also, since the model of a plane wave with slowly varying parameters comes from an assumed eikonal variation $\exp(iS)$ with $\omega = -\partial S/\partial t$ and $k_\| = \partial S/\partial\zeta$, we have $\partial k_\|/\partial t = -\partial\omega/\partial\zeta \approx (\partial\omega/\partial t)/V_{g\|}$.

4.2 Terms Involving Spatial Dependence

From equation 3, $k_\|$ can be treated as a function of $(\omega_{pe}, \Omega_e, \omega, \theta)$. The variation with θ is often neglected (Albert, 2000; Omura et al., 2008; Mourenas et al., 2015) but this is questionable for highly oblique waves, since the corresponding n is highly sensitive to θ.

For constant ω, Bell (1984) essentially wrote

$$\frac{\partial k_\|}{\partial \zeta} = \frac{\partial k_\|}{\partial \omega_{pe}}\frac{\partial \omega_{pe}}{\partial \zeta} + \frac{\partial k_\|}{\partial \Omega_e}\frac{\partial \Omega_e}{\partial \zeta} + \frac{\partial k_\|}{\partial \omega}\frac{\partial \omega}{\partial \zeta} + \frac{\partial k_\|}{\partial \theta}\frac{\partial \theta}{\partial \zeta} \tag{17}$$

and cited an expression for $\partial\theta/\partial\zeta$ derived from the ray tracing equations, though it was noted that it strictly applied along the wave trajectory, not the particle path. Bell (1986) actually traced multiple rays, found field line crossings, and evaluated $\partial\theta/\partial\zeta$ from fitting and finite differencing. Here, since the trajectories of highly oblique waves are nearly field-aligned, $\partial k_\|/\partial\zeta$ and $\partial\Omega_e/\partial\zeta$ are obtained by directly finite-differencing along the trajectory of a single traced ray.

4.3 Evaluation

We consider waves at $L = 2$, with frequency near the lower hybrid frequency and wave normal angle between the Gendrin and resonance cone values. Then the refractive index is large but $k_\|$ is small, and the resonance condition with $|\ell| = 1$ or larger requires large values of $v_\|$, hence large particle energy. More concretely, the wave parameters $\omega \approx \omega_{LH}$ and $\theta \approx \theta_G$ lead to the estimate $p_\|/mc = 25|n|(\Omega_e/\omega_{pe})$, or energy in the MeV range. The number of such energetic electrons is likely too low to account for triggered emissions, so only the Landau resonance, $\ell = 0$, is considered. The corresponding estimate is $v_\|/c = 0.5(\Omega_e/\omega_{pe})$, or typical energy in the keV range. For Landau resonance $v_\|$ has the same sign as $k_\|$ which, as mentioned above, has the same sign as $V_{g\|}$; thus the resonant wave and particle co-propagate up or down the field line.

For a representative evaluation, we take the cold plasma density at $L = 2$ to be $n_e = 2850$ cm^{-3}, so that the plasma frequency is $f_{pe} = 480.46$ kHz, the equatorial electron cyclotron frequency is $f_{ce} = 108.50$ kHz, and the lower hybrid frequency is $f_{LH} = 2.47$ kHz. The wave frequency is taken to be 1.1 f_{LH}, giving a resonance cone angle of $\theta_{RC} = 89.39°$ and Gendrin angle of $\theta_G = 88.66°$. The initial wave normal angle θ is set to $(\theta_{RC}+\theta_G)/2$, with the $\mathbf{k}$ vector pointing earthward relative to the geomagnetic field line. This gives initial values $kc/\omega \approx 390$ and wavelength of 280 m. Upon ray tracing in a simple dipole, Figure 9 shows that the wave stays very nearly on the same field line, with θ increasing through 90◦ while the wave reflects at about 12° latitude. The refractive index increases to about 420 during the upward leg and decreases during the downward leg, while $|k_\||$ does the reverse. It takes about half a second for the wave to reflect and return to the equator.

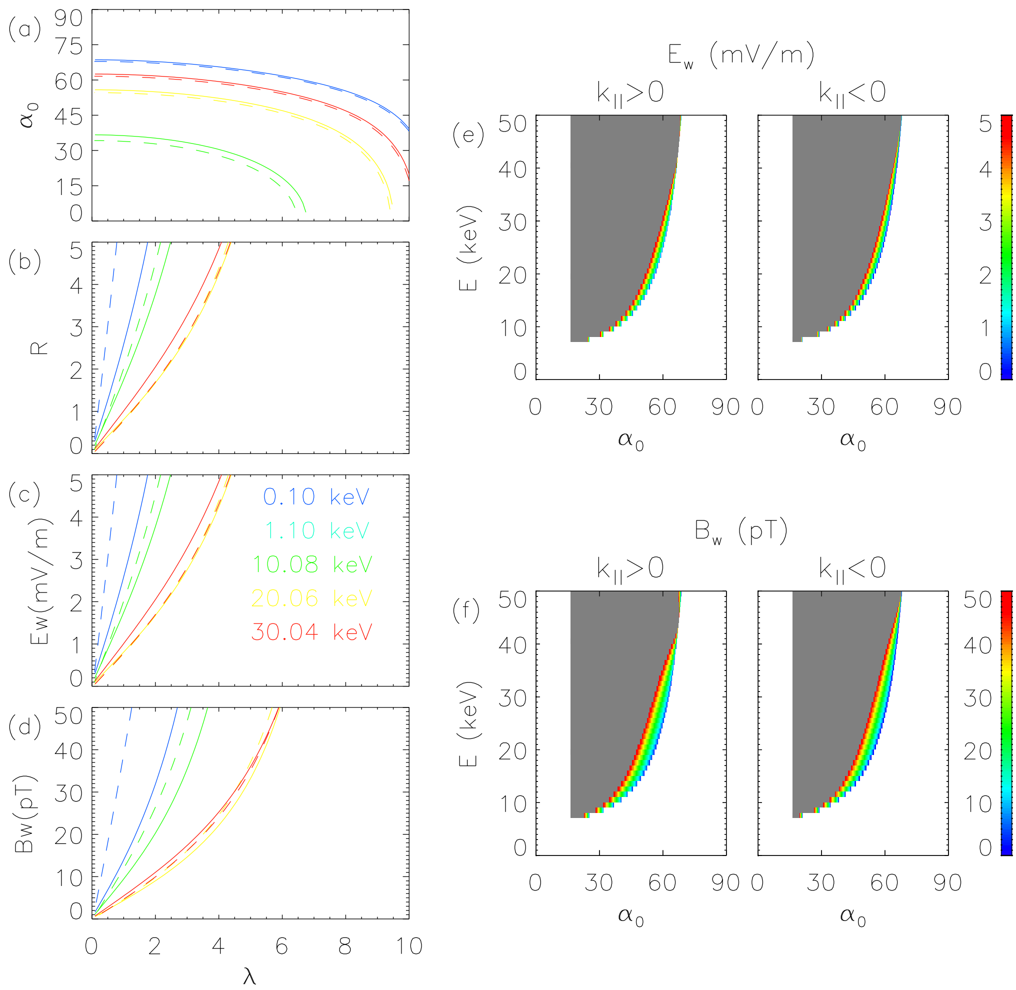

Figure 10. (a) Resonant value of equatorial pitch angle α_0, and (b) inhomogeneity parameter R at resonance vs. latitude for the traced wave shown in Figure 9, assuming a constant wave electric field $E_w = 1$ mV/m, for electrons with energy approximately 0.1, 1, 10, 20, and 30 keV. (c) The wave electric field and (d) wave magnetic field required to scale the inhomogeneity parameter to $R = 1$. the solid curves show values for the upward leg of the wave path (with $V_{g\|}$ and $k_\|$ positive), and dashed curves show values for the return path (with $V_{g\|}$ and $k_\|$ negative). The wave electric and magnetic field required to scale to $R = 1$ are shown in (e) and (f) as functions of resonant particle energy and α_0.

The inhomogeneity parameter R was evaluated along the traced ray path by first specifying the particle energy E, and determining the corresponding pitch angle at each location using the resonance condition (the right hand side of Equation 9 set to 0, with $\ell = 0$). The equatorial value, α_0, is shown in panel (a) of Figure 10 for several values of energy in the keV range. The upward and downward legs of the wave path (solid and dashed curves, respectively) are treated separately. Figure 10b shows R from Equation 11, assuming $\partial\omega/\partial t = 0$. The wave electric field amplitude at each location was assumed to be 1 mV/m. Values $R < 1$, indicating nonlinear particle motion that could participate in generating triggered emissions, were reached at low latitude. Figures 10c and 10d show what values of wave electric and magnetic field, respectively, would be needed to scale the inhomogeneity parameter to $R = 1$ for each combination of E and λ. Figures 10e and 10f show the same required wave fields for a wide range of E and α_0 values, and generally indicate that waves with electric field in the mV/m range and magnetic fields of a few 10s of pT, are sufficient to induce nonlinear behavior through Landau resonance with some particles with energy of 10s of keV.

5 Summary

The DSX mission represents a rare and exciting active space experiment in which a high-power VLF transmitter excited propagating electromagnetic waves. These waves were received by remote spacecraft, reflected back to DSX, and may have been sufficiently intense to produce trigger emissions. Application of well-validated ray tracing techniques in cold and warm plasmas paints a picture of unusually oblique wave normals excited over a very limited range of angles to the geomagnetic field, which should reveal details about the DSX antenna pattern. In addition, analysis of any observed triggered emissions will help to constrain wave intensities, possibly pointing toward linear amplification as a mechanism for achieving the substantial wave intensities required for nonlinear wave-particle interactions. Detailed analysis of the DSX data set is currently underway.

Open Research

Data collected from the DSX mission is undergoing post-mission processing and quality control. When this process is complete, it will become available without restrictions via the NASA Space Physics Data Facility. A freely available ray tracing package is available at https://github.com/rareid2

Acknowledgments

This work was supported by AFOSR grant 22RVCOR002 and the Space Vehicles Directorate of the Air Force Research Laboratory. The DSX spacecraft was built and operated by the Air Force Research Laboratory with launch services provided by the Space Test Program at Space Systems Command. We thank the DSX BBR team (Umran S. Inan, Ivan Linscott) and the DSX VLF transmitter team (Bodo Reinisch, Paul Song, Ivan Galkin) for their roles in acquiring the DSX data shown herein.

References

Albert, J. M. (1993). Cyclotron resonance in an inhomogeneous magnetic field. *Physics of Fluids B*, *5*, 2744-2750. Retrieved from https://doi.org/10.1063/1.860715

Albert, J. M. (2000). Gyroresonant interactions of radiation belt particles with a monochromatic electromagnetic wave. *Journal of Geophysical Research*, *105*, 21,191-21,209. Retrieved from https://doi.org/10.1029/2000JA000008

Albert, J. M. (2005). Evaluation of quasi-linear diffusion coefficients for whistler mode waves in a plasma with arbitrary density ratio. *Journal of Geophysical Research*, *110*, A03218. Retrieved from https://doi.org/10.1029/2004JA010844

Albert, J. M. (2007). Simple approximations of quasi-linear diffusion coefficients. *Journal of Geophysical Research*, *112*, A12202. Retrieved from https://doi.org/10.1029/2007JA012551

Albert, J. M. (2008). Efficient approximations of quasi-linear diffusion coefficients in the radiation belts. *Journal of Geophysical Research*, *113*, A06208. Retrieved from https://doi.org/10.1029/2007JA012936

Albert, J. M. (2017). Quasi-linear diffusion coefficients for highly oblique whistler-mode waves. *Journal of Geophysical Research Space Physics*, *122*, A00F05. Retrieved from https://doi.org/10.1029/2017JA024124

Albert, J. M., Tao, X., & Bortnik, J. (2013). Aspects of nonlinear wave-particle interactions. In *Dynamics of the Earth's Radiation Belts and Inner Magnetosphere* (p. 255-264). American Geophysical Union (AGU). Retrieved from https://agupubs.onlinelibrary.wiley.com/doi/abs/10.1029/2012GM001324 doi: 10.1029/2012GM001324

Alken, P., E., T., Beggan, C. D., H., A., Aubert, J., Baerenzung, J., & et al. (2021). International geomagnetic reference field: the thirteenth generation. *Earth Planets and Space*, *7*, 49. Retrieved from https://doi.org/10.1186/s40623-020-01288-x

Aryan, H., Sibeck, D., Balikhin, M., Agapitov, O., & Kletzing, C. (2016). Observation of chorus waves by the van allen probes: Dependence on solar wind parameters and scale size. *Journal of Geophysical Research Space Physics*, *121*, 7608-7621. Retrieved from https://doi.org/10.1002/2016JA022775

Aubrey, M. P., Bitoun, J., & Graff, P. (1970). Propagation and group velocity in a warm magnetoplasma. *Radio Science*, *5*, 635.

Bell, T. F. (1984). The nonlinear gyroresonance interaction between energetic electrons and coherent VLF waves propagating at an arbitrary angle with respect to Earth's magnetic field. *Journal of Geophysical Research*, *89*, 905-918. Retrieved from https://doi.org/10.1029/JA089iA02p00905

Bell, T. F. (1986). The wave magnetic field amplitude threshold for nonlinear trapping of energetic gyroresonant and Landau resonant electrons by nonducted VLF waves in the magnetosphere. *Journal of Geophysical Research*, *91*, 4365-4379. Retrieved from https://doi.org/10.1029/JA091iA04p04365

Budden, K. (1988). *The Propagation of Radio Waves: The Theory of Radio Waves of Low Power in the Ionosphere and Magnetosphere.* Cambridge University Press.

Cohen, M., Lehtinen, N., & Inan, U. S. (2012). Models of ionospheric VLF absorption of powerful ground based transmitters. *Geophysical Research Letters*, *39*. Retrieved from https://doi.org/doi:10.1029/2012GL054437

Colman, J. J., & Starks, M. J. (2013). VLF wave intensity in the plasmasphere due to tropospheric lightning. *Journal of Geophysical Research: Space Physics*, *118*, 4471-4482.

Gendrin, R. (1961). Le guidage des whistlers par le champ magnetique. *Planetary and Space Science*, *5*, 274.

Gołkowski, M., Harid, V., & Hosseini, P. (2019). Review of controlled excitation of non-linear wave-particle interactions in the magnetosphere. *Frontiers in Astronomy and Space Sciences*, *6*. Retrieved from `https://doi.org/10.3389/fspas.2019.00002`

Haselgrove, J. (1963). The Hamilton ray path equations. *Journal of Atmospheric and Terrestrial Physics*, *25*, 397.

Helliwell, R. (1965). *Whistlers and Related Ionospheric Phenomena.* Palo Alto: Stanford University Press.

Helliwell, R. A., & Katsufrakis, J. P. (1979). Vlf wave injection into the magnetosphere from Siple Station, Antarctica. *Journal of Geophysical Research*, *79*, 2511. Retrieved from `https://doi.org/10.1029/JA079i016p02511`

Inan, U. S., & Bell, T. F. (1977). The plasmapause as a VLF waveguide. *Journal of Geophysical Research*, *82*, 2819. Retrieved from `https://doi.org/10.1029/JA082i019p02819`

Inan, U. S., Chang, H. C., & Helliwell, R. A. (1984). Electron precipitation zones around major ground-based VLF signal sources. *Journal of Geophysical Research*, *89*, 2891-2906. Retrieved from `https://10.1029/JA089iA05p02891`

Kimura, I. (1966). Effects of ions on whistler-mode ray tracing. *Radio Science*, *1*, 269-283.

Li, J. D., Spasojevic, M., & Inan, U. S. (2015). An empirical profile of vlf triggered emissions. *Journal of Geophysical Research Space Physics*, *120*, 6581-6595. Retrieved from `https://doi.org/10.1002/JA021444`

Li, W., Ma, Q., Thorne, R., Bortnik, J., Kletzing, C., Kurth, W., ... Nishimura, Y. (2015). Statistical properties of plasmaspheric hiss derived from van allen probes data and their effects on radiation belt electron dynamics. *Journal of Geophysical Research Space Physics*, *120*, 3393-3405. Retrieved from `https://doi.org/10.1002/2015JA021048`

Linscott, I., Inan, U. S., Lauben, D. S., Farrell, W. M., Payne, J., Mossiwir, B., ... Su, Y.-J. (2022). The Broad Band Receiver (bbr) payload. *Journal of Geophysical Research Space Physics*.

Marshall, R. A., Sousa, A., Reid, R., Wilson, G., Starks, M., Ramos, D., ... Inan, U. S. (2021). The Micro-Broadband Receiver (μBBR) on the Very-low-frequency Propagation Mapper cubesat. *Earth and Space Science*, *8*. Retrieved from `https://doi.org/10.1029/2021EA001951`

Maxworth, A. S., & Gołkowski, M. (2017). Magnetospheric whistler mode ray tracing in a warm background plasma with finite electron and ion temperature. *Journal of Geophysical Research Space Physics*, *122*, 7323-7335. Retrieved from `https://doi.org/10.1002/2016JA023546`

McCollough, J. P. I., Miyoshi, Y., Ginet, G. P., Johnston, W. R., Su, Y.-J., Starks, M. J., ... Langhals, J. T. (2022). Space-to-space very low frequency radio transmission in the magnetosphere using the DSX and Arase satellites. *Earth, Planets and Space*.

Meredith, N. P., Horne, R. B., Kersten, T., Li, W., Bortnik, J., Sicard, A., & Yearby, K. (2018). Global model of plasmaspheric hiss from multiple satellite observations. *Journal of Geophysical Research Space Physics*, *123*, 4526-4541. Retrieved from `http://doi.org/10.1029/2018JA025226`

Meredith, N. P., Horne, R. B., Shen, X.-C., Li, W., & Bortnik, J. (2020). Global model of whistler mode chorus in the near-equatorial region ($|\lambda_m| < 18°$). *Geophysical Research Letters*, *47*. Retrieved from `http://doi.org/10.1029/2020GL087311`

Mourenas, D., Artemyev, A. V., Agapitov, O. V., Krasnoselskikh, V., & Moser, F. S. (2015). Very oblique whistler generation by low-energy electron streams. *Journal of Geophysical Research Space Physics*, *120*, 3655-3683. Retrieved from `https://doi.org/10.1029/2015JA021135`

Omura, Y., Katoh, Y., & Summers, D. (2008). Theory and simulation of the generation of whistler-mode chorus. *Journal of Geophysical Research*, *113*, A04223. Retrieved from https://doi.org/10.1029/2007JA012622

Reid, R., Marshall, R. A., Starks, M. J., Usanova, M. E., Wilson, G. R., Johnston, W. R., . . . Galkin, I. A. (2022). Active VLF transmission experiments between the DSX and VPM spacecraft. *Journal of Geophysical Research Space Physics*.

Reinisch, B. W., Haines, D. M., Bibl, K., Cheney, G., Galkin, I. A., Huang, X., . . . Reiff, P. (2000). The Radio Plasma Imager investigation on the IMAGE spacecraft. *Space Science Reviews*, *91*, 319-359. Retrieved from https://doi.org/10.1023/A:1005252602159

Reinisch, B. W., Song, P., Galkin, I. A., Stelmash, S. S., Roche, K., Khmyrov, G. M., & et al. (2022). The VLF transmitter, narrow-band receiver, and tuner investigation on the DSX spacecraft. *Journal of Geophysical Research Space Physics*.

Scherbarth, M., Smith, D., Adler, A., Stuart, J., & Ginet, G. (2009). AFRL's Demonstration and Science Experiments (DSX) mission. In S. Fineschi & J. A. Fennelly (Eds.), *Solar physics and space weather instrumentation iii* (Vol. 7438, p. 101-110). SPIE. Retrieved from https://doi.org/10.1117/12.824898

Smith, R. (1961). Propagation characteristics of whistlers trapped in field-aligned columns of enhanced ionization. *Journal of Geophysical Research*, *66*, 3699.

Starks, M. J. (2002). Effects of hf heater-produced ionospheric depletions on the ducting of VLF transmissions: A ray tracing study. *Journal of Geophysical Research*, *107*, 1336.

Starks, M. J., Albert, J. M., Ling, A., O'Malley, S., & Quinn, R. (2020). VLF transmitters and lightning-generated whistlers: 1. modeling waves from source to space. *Journal of Geophysical Research Space Physics*, *125*. Retrieved from https://doi.org/10.1029/2019JA027029

Starks, M. J., Quinn, R. A., Ginet, G. P., Albert, J. M., G., S., Reinisch, B., & Song, P. (2008). Illumination of the plasmasphere by terrestrial very low frequency transmitters: Model validation. *Journal of Geophysical Research Space Physics*, *113*. Retrieved from http://doi.org/10.1029/2008JA013112

Stix, T. H. (1992). *Waves in Plasmas.* New York: American Institute of Physics.

Storey, L. R. O. (1953). An investigation of whistling atmospherics. *Philosophical Transactions of the Royal Society of London, Series A*, *246*, 113-141.

Tao, X., Zonca, F., Chen, L., & Wu, Y. (2020). Theoretical and numerical studies of chorus waves: A review. *Science China Earth Sciences*, *63*, 78-92. Retrieved from https://doi.org/10.1007/s11430-019-9384-6